# Parametric studies of effects of finite pixel and AOI sizes on the accuracy of Shack-Hartmann WFS

Ethan D. Chu[a] and Stanislav Gordeyev[a]

[a]University of Notre Dame, Notre Dame, IN, United States

## ABSTRACT

In previous work, we studied the effects of a supersonic shockwave on the performance of a Shack-Hartmann wavefront sensor (SHWFS). A shockwave is a sudden change in density which then cause a sharp gradient in the wavefront. This results in dots distorting in the SHWFS dot pattern which in turn affects the accuracy of wavefront reconstruction. We used higher order statistics, such as standard deviation, skewness and kurtosis to identify and eliminate these distorted dots in Shack-Hartmann wavefront sensors, improving the accuracy of the final reconstructed wavefront. However, this is contingent on accurate calculations of the centroid, standard deviation, skewness, and kurtosis of these dots. In the first part of this work, we look at the effect of the finite pixel size on the accuracy of the Shack-Hartmann wavefront sensor, specifically on the calculation of the centroid and higher order statistics of a pixelated dot. We simulate a dot and average the intensity distribution for different pixel sizes. We show that the error is significant if the ratio of the center Dot size/pixel size is less than 2. Past this ratio of 2, the centroid and statistics error of the dots drop to near zero. We also explain some striping artifacts observed in the statistics maps in experimental work. In the second part of this paper, we investigate the centroid error of a dot approaching the edge of the Area of Interest (AOI). In cases of large tilts in the wavefronts, the dot can be pushed into or past the edge of the AOI. We show that a large AOI size/Dot size ratio allows for the most tilt and range of movement. However, by squaring or cubing the intensity distribution, the error can be further reduced for a given system.

## 1. INTRODUCTION

The Shack-Hartmann Wavefront Sensor (SHWFS) is an extremely useful and versatile tool for measuring the wavefront of a light source. Its application is used across multiple industries including aerospace. In previous work,[1] we looked at the effects of supersonic shocks on the SHWFS, specifically on how the shocks-related sharp wavefront gradients bifurcate or distort the dots. These distorted dots prevent accurate calculation of the centroid positions which then affect the reconstruction process. We showed that removing these distorted dots improves the final reconstructed wavefront by comparing the wavefronts to a Digital Holography wavefront sensor (DHWFS). To identify these dots we used the standard deviation ($\sigma$), and kurtosis ($Kurt$) of the dot intensity pattern as well as slope discrepancy to identify these distorted dots and eliminate them with a simple threshold. However, when calculating the $\sigma$ and $Kurt$ maps, we observed a stripe pattern that appear in the analysed 2-D maps, which were not related the flow features. Figure 1 shows examples of these stripes that appear on these statistics maps for both no-flow case, shown in Figure 1(a-d), as well as flow-on case, Figure 1(e-h).

To investigate these artifacts, we performed extensive parametric studies and demonstrated that the stripe pattern is the result of the finite pixel size on a digital camera, as well as finite lenslet array pitch. In Section 2, we study how the pixelation (a finite pixel size) effect of a diffraction limited dot affects the centroid, $\sigma$, and $Kurt$ calculations. The question that we seek to answer in this study is what resolution is needed to accurately measure the centroid and higher order statistics? And does this explain the stripes that we see in the $\sigma$ and $Kurt$ maps?

In Section 3, we analyze the error associated with a dot that is approaching or situated at the edge of the Area of Interest (AOI). Supersonic shocks create sudden changes in density, resulting in a steep gradient in the wavefront. This causes the dots to deflect significantly towards the edge of the AOI. Thus part of the dot intensity pattern, specifically the tails, is outside the AOI. Consequently, this impacts centroid calculations as part of the dot pattern is excluded from the calculations. Here, we examine the errors linked to a dot nearing or crossing the AOI boundary.

Unconventional Imaging, Sensing, and Adaptive Optics 2024, edited by Jean J. Dolne, Santasri R. Bose-Pillai, Matthew Kalensky, Proc. of SPIE Vol. 13149, 131490C
© 2024 SPIE · 0277-786X · doi: 10.1117/12.3027809

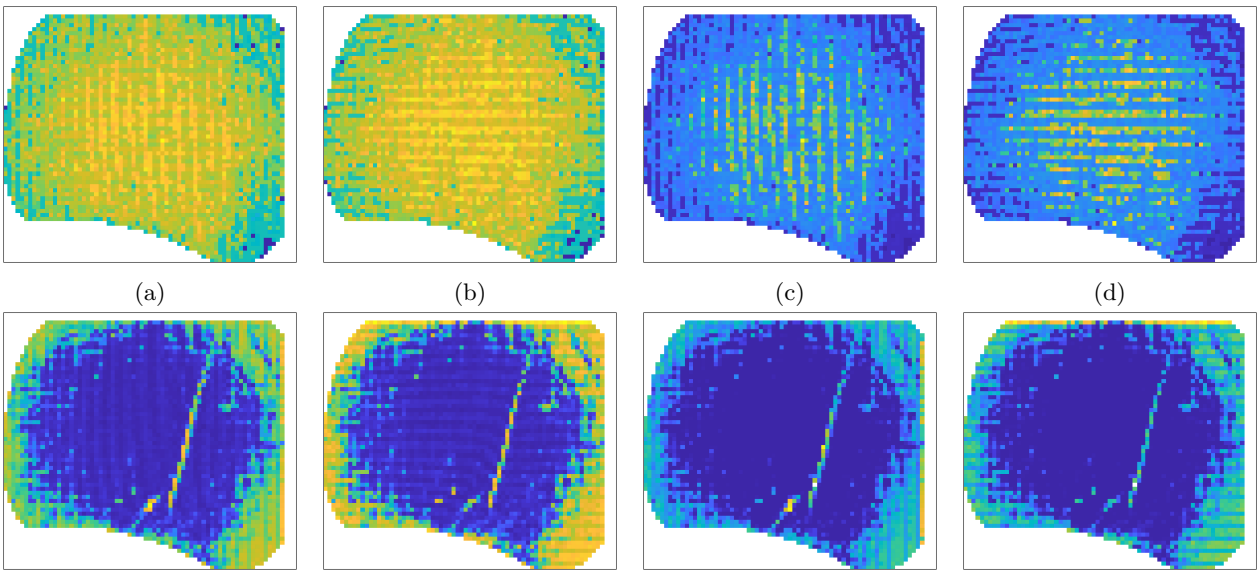


Figure 1: (a) $\sigma_x$, (b) $\sigma_y$, and (c) $Kurt_x$, (d) $Kurt_y$ maps of the dot pattern in a no-flow condition. (e) $\sigma_x$, (f) $\sigma_y$, and (g) $Kurt_x$, (h) $Kurt_y$ maps in a supersonic flow, showing the higher values of $\sigma$ and $Kurt$ values over the shock location

## 2. SHACK-HARTMANN PIXELATION EFFECTS

### 2.1 SHWFS Wavefront Reconstruction

The main principle behind Shack-Hartmann WFS is an lenslet array which creates a grid of dots at the focal plane of the lenslets. This resulting image is usually captured by a digital image sensor. The wavefront is then calculated by calculating the displacement of the dots with the Area of Interest (AOI). The AOI is most commonly defined by the size of the lenslet array (i.e. the AOI has the same size as the lenslet array). Generally, the centroid location is calculated for both x- and y-directions; however, for this study we calculate the centroid's x-location only to reduce computational time and simplify the problem. A two-dimensional analysis was done to confirm that the y-location does not affect the presented analysis. The x-location of the centroid is defined as Equation 1.[2]

$$\overline{x} = \frac{\sum_{n=1}^{\infty} I(x_n, y_m)\, x_n}{\sum_{n=1}^{\infty} I(x_n, y_m)} \tag{1}$$

where $I(x_n, y_n)$ is the intensity of each pixel, $x_n, y_m$ is the location of the pixel within the AOI, and $\overline{x}$ is the relative location of the centroid. This is also sometimes referred to as the first moment of the intensity distribution within the AOI. The slope of the wavefront is then estimated using Equation 2

$$\left(\frac{\partial w}{\partial x}\right) \approx -\frac{\Delta x}{f} \tag{2}$$

where $\left(\frac{\partial w}{\partial x}\right)$ is the one-dimensional wavefront slope over a subaperture lenslet, $\Delta x$ is the deflection of the centroid from the center of the AOI, and $f$ is the lenslet focal length. Again, this is only for the displacement in x-direction. For this study, we used slope rather than centroid shift as this value is more universally useful than an absolute shift of the centroid. This gives us the approximation of the slope or tilt of the wavefront that is associated with the shift in the centroid.

In this study we are interested in the pixelation effect on the camera sensor. Thus it is important to know the size of the dot as well as the camera pixel size. The half-width of the dot for a square aperture is calculated by Eq. 3

$$W_x = \frac{\lambda f}{L_{AOI}} \tag{3}$$

where $W_x$ is the half-width of the beam at the observation plane, $\lambda$ is the wavelength, $f$ is the focal length of the lenslet, and $L_{AOI}$ is the width of the aperture/lenslet.[3] For this study, we introduce a new parameter called the dot/pixel ratio, $\zeta_{pixel}$

$$\zeta_{pixel} = \frac{2W_x}{L_{pixel}} \tag{4}$$

where $L_{pixel}$ is the size of the pixel in meters. This ratio defines how many pixels are needed to fully capture the center peak. For example, $\zeta_{pixel} = 2$ would mean that 2 pixels would capture the center peak of the dot. For reference, our experimental setup in our previous work[1] would have a dot width of about $135\mu m$. Using a camera with a pixel size of $28\mu m$, a diffraction limited dot would be about 4.8 pixels across. However, once the background noise is eliminated from the image, often times, only 2-4 pixels are left to calculate the centroid. Fig. 2 shows an example of these dots. Fig. 3a is a simulation of a diffraction limit dot with a grid overlayed on it, representing the pixel divisions. Fig. 3b shows the pixel averaging of the dot, very similar to what we see in Fig. 2.

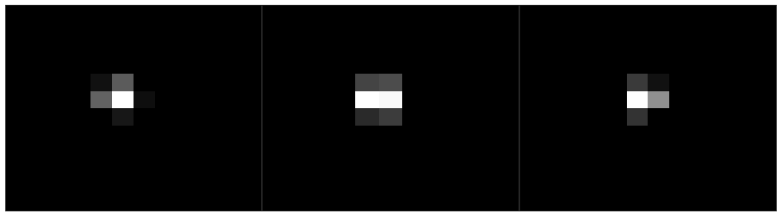
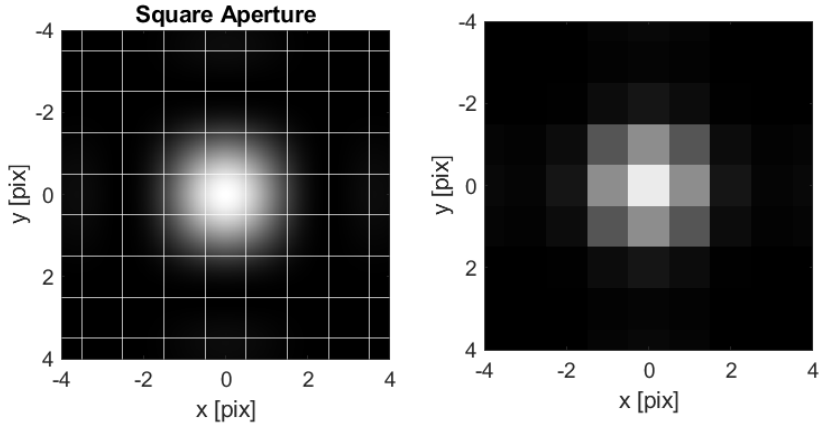


Figure 2: Typical diffraction limited dots which are only 2-4 pixels across.




(a) (b)

Figure 3: (a) A simulation of a diffraction limited dot with a pixel grid overlayed on top. (b) The dot is averaged across the pixels as defined by the pixel grid.

In the previously mentioned study,[1] we explored the effect of supersonic shockwaves on the SHWFS, specifically how the presence of the shockwave distorts the dot pattern. We used higher order statistics of the dot intensity, specifically standard deviation and kurtosis, to identify these dots and remove them during the wavefront reconstruction process. These statistics describe how "distorted" the dot is. By comparing the statistics of a diffraction limited dot to a distorted dot, we can identify and remove the distorted dots with a simple threshold. Equation 5 defines the second moment or more commonly known as standard deviation.

$$\mu_{2,x} = \frac{\sum_{n=1}^{\infty} I(x_n, y_m)\,(x_n - \overline{x})^2}{\sum_{n=1}^{\infty} I(x_n, y_m)} \quad \text{and} \quad \sigma_x = \sqrt{\mu_{2,x}} \tag{5}$$

where $\mu_{2,x}$ is the second central moment in $x$ and $\sigma_x$ is the standard deviation beam width in $x$. This quantity represents the relative width of the intensity distribution in the $x$ direction. For completeness, we also include the third central moment or skewness

$$\mu_{3,x} = \frac{\sum_{n=1}^{\infty} I(x_n, y_m)\,(x_n - \overline{x})^3}{\sum_{n=1}^{\infty} I(x_n, y_m)} \quad \text{and} \quad Skew_x = \frac{\mu_{3,x}}{\sigma_x^3} \tag{6}$$

where $\mu_{3,x}$ is the third central moment and $Skew_x$ is the skewness in $x$. Skewness is more the description of how much the peak is shifted from the mean. In our study in Ref. 1, we did not use skewness as we were not so much concerned with the symmetry of the distribution but with the overall intensity distribution in the AOI. Other studies have explored using skewness and higher order statistics to improve wavefront reconstruction for SHWFS.[4]

The fourth central moment or kurtosis is used to identify the "tailedness" of the distribution, (i.e. a measure that relates to the tails of a distribution). Higher kurtosis values indicate a greater presence of extreme deviations (or outliers) in the data. In the presence of a sharp gradient, the dots are usually distorted in some extreme fashion which increases the presence of these outliers. Kurtosis allows us to quantify the "spread" of the distribution for these distorted dots. This is defined as

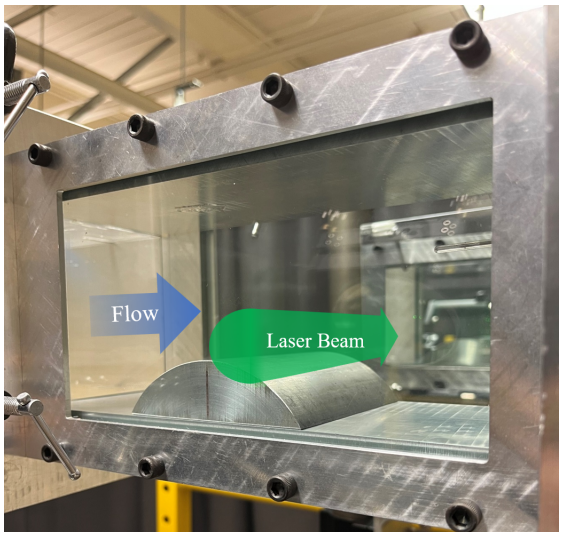
$$\mu_{4,x} = \frac{\sum_{n=1}^{\infty} I(x_n, y_m)\,(x_n - \overline{x})^4}{\sum_{n=1}^{\infty} I(x_n, y_m)} \quad \text{and} \quad Kurt_x = \frac{\mu_{4,x}}{\sigma_x^4} \tag{7}$$

where $\mu_{4,x}$ is the fourth central moment and $Kurt_x$ is the kurtosis in $x$. In further discussions, $\mu_4$ refers to the fourth central moment and $Kurt$ as the relative kurtosis as it has been normalized by $\sigma$.

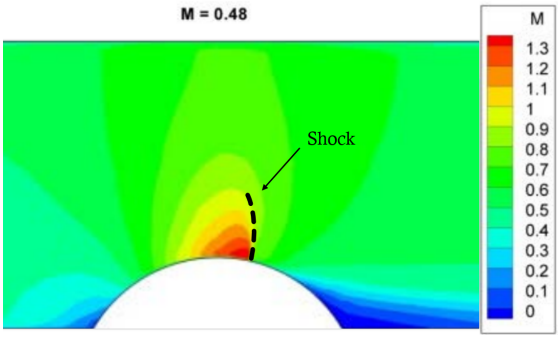
### 2.2 Experimental Setup

In our previous work,[1] we studied the effects of a supersonic shockwave on the SHWFS and DHWFS. These experiments were performed at the Hessert Laboratory for Aerospace Research at the University of Notre Dame. A partial cylinder was placed in a indraft wind tunnel which constructs the flow and accelerates the flow to just past supersonic as it passes over the top of the flow. Fig. 4a shows the physical setup of the cylinder in the wind tunnel. Fig. 4b shows the velocities of the flow as the air passes over the cylinder and the expected location of the shock as the flow reaches supersonic speeds.

A simultaneous SHWFS and DHWFS setup was used to capture the shock. The purpose was to compare the two wavefronts when a shock was in frame. Due to this sudden change in density, the shock causes a sharp gradient in the wavefont which results with the dots on the SHWFS to smear or bifurcate.[6–9] Since the dot is distorted, the centroid equation, Eq. 1, is no longer applicable. The DHWFS can be captured at much higher resolutions thus it is still able to reconstruct the steep gradient of the wavefront. This allows us to test the accuracy of the SHWFS before and after removing the distorted dots. For the SHWFS, we used a v1611 Phantom High-Speed camera with a max resolution of 1280x800 and a pixel size of $28\mu m$. A 72x72 lenslet array is attached to the camera and uses square lenslets of 0.3 x 0.3 mm with a focal length of 38 mm. A 532 nm laser is used as the illumination source. The DHWFS uses a v1840 Phantom High-Speed camera with a max resolution of 2048x1952 and a pixel size of $13.5\mu m$. More details about the test setup can be found in Ref. 1.




(a)




(b)

Figure 4: (a) Tunnel test section with 2-D partial cylinder. (b) CFD simulation[5] showing transonic flow over partial cylinder with shock marked by dashed line.

### 2.3 Procedure

In our simulations, we approximated dot's intensity pattern using a double sinc function, since we use a lenslet array with square lenslets. The irradiance is defined as Eq. 8.

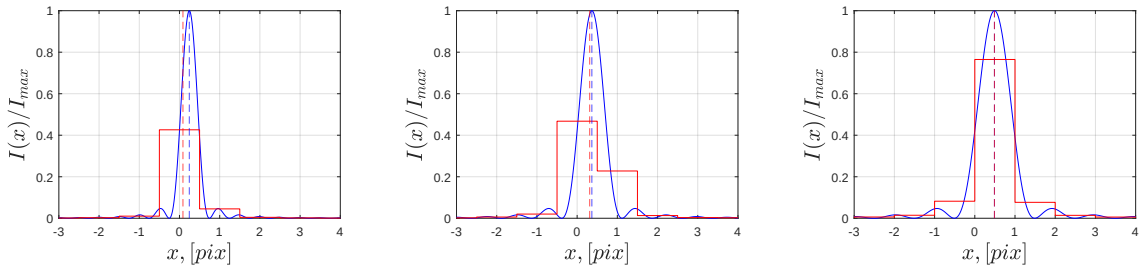
$$I(x,y) = \left(\frac{L_{AOI}^2}{\lambda f}\right)^2 sinc\left(\frac{L_{AOI}\ x}{\lambda f}\right)^2 sinc\left(\frac{L_{AOI}\ y}{\lambda f}\right)^2 \tag{8}$$

where $I(x,y)$ is the intensity distribution of a diffraction limited dot, $L_{AOI}$ is the size of the square aperture of the lenslet which also defines the size of the AOI, $\lambda$ is the wavelength of the laser, $f$ is the focal length of the lenslet, and $x$ and $y$ is the location across the lenslet. This equation is for two-dimensions, but shifts in the $x$-direction and $y$-direction are independent of each other. To simplify this study and improve computational speed, only shifts in the x-direction were studied.

Different pixel sizes were then selected and the diffraction limited dot is then averaged across these pixels. Shifting the irradiance pattern across the x-axis simulates the movement of the dot across the AOI, changing the averaged intensity distribution as the dot moves between pixels. The centroid, $\sigma$, and $Kurt$ is calculated for each shift and compared to the diffraction limited dot. The diffraction limited dot would have a constant centroid, $\sigma$, and $Kurt$ values as the dot moves across the AOI. Large pixels will have the highest error, while smaller and smaller pixels would converge towards the diffraction limit dot intensity distribution. Because we are using a double sinc function, the center dot is not the same as the Airy's disk but is similar. In further discussions, we will refer to this center peak as the Dot peak.

### 2.4 Results and Discussions

Fig. 5 shows the pixelation effects of a diffraction limited dot at $\zeta_{pixel} = 1$, 1.5, and 2. The dot is shifted in $x$-direction which has units of pixels and zero is the center of the AOI. Fig. 5 shows the true centroid of the dot is shifted part way across the pixel. We can see how the different sizes of the pixels changes the averaged intensity distribution. Fig. 5a shows the case of $\zeta_{pixel} = 1$ where one pixel is the size of the dot width. The blue dotted line shows the true centroid of the dot and is in between pixels. The red dotted line shows the centroid as calculated by the averaged pixelated intensity. In this case of $\zeta_{pixel} = 1$, red dotted line is visibly off the true centroid. Fig. 5b and 5c show that increasing $\zeta_{pixel}$ visibly improves the position of the calculated centroid.




(a) (b) (c)

Figure 5: The intensity distribution showing the averaged intensity (red) of a diffraction limited dot (blue) of a $\zeta_{pixel}$ of (a) 1, (b) 1.5, and (c) 2. The blue dotted line shows the centroid of the diffraction limited dot, (i.e.the true centroid).

The error is calculated as the difference between calculated centroid of the averaged pixelated intensity distribution ($Tilt_{calculated}$) and the true centroid of the dot $Tilt_{true}$, $Tilt_{error} = Tilt_{calculated} - Tilt_{true}$. Figure 6a plots the error of centroid as the dot moves left to right, and we can clearly see an oscillating pattern. This oscillating pattern is expected as the "weight" of the averaged intensity as dot shifts more drastically across the pixels at low $\zeta_{pixel}$ values than at high $\zeta_{pixel}$ values. Figures 6b and 6d shows the relative error of $\sigma$ and $Kurt$ which also show this oscillation back and forth. The location of the maximum error of both $\sigma$ and $Kurt$, occurs when the dot is at multiples of half a pixel (i.e. the dot is in between pixels). It is also interesting to note that these peaks occur at the point where the centroid error is the smallest. $Skew$ plot behaves a little more erratically because it is sensitive to location of the centroid and the distribution shape. Since skewness is measuring is the asymmetry around the centroid, the shifting pixels heavily affects the symmetry of the intensity distribution. The first few points of the $Skew$ plot were not included as these often blew up to very large numbers. This is because the $Skew$ of the diffraction limited dot is basically zero, where even a small increase of skewness in the pixelated intensity would blow up the relative error.

In Figures 7a, 7b, 7c, and 7d show the RMS error and maximum absolute error for centroid shift/tilt, $\sigma$, $Skew$, and $Kurt$, respectively. The error plots were simulated for $\zeta_{pixel}$ values of 0.8 to 8. The tilt error drops to essentially zero at $\zeta_{pixel} = 2$, which suggests that for all practical purposes, as long there are at least two pixels for the Airy's or Dot size, the centroid can be accurately calculated. $\sigma$ and $Kurt$ error also decreases at a predictable rate. It is also interesting to note that at $\zeta_{pixel} = 2$ there is also an noticeable jump in improvement for $\sigma$ and $Kurt$. The $Skew$ error does not appear to have this jump but does have a decreasing trend.

### 2.5 Origin of Stripe Pattern

The second goal of this pixelation study was to explain the presence of the stripe pattern seen in Fig. 1. Our SHWFS experimental setup uses lenslets of $300\mu m$ and the camera has a pixel size of $28\mu m$, which means each AOI contains 10.7 pixels. Because of this slight mismatch between the pixel size and AOI, it causes the projected dot to be slightly mismatched with the pixels as well. Thus the intensity distribution is not always centered on the pixels. This creates an uneven distribution across some of the pixels. Fig. 8a shows a simulation where that intensity distribution is not perfectly centered on each AOI. This slight offset then creates a bias in the statistics. Magnifying Fig. 1c, we see the stripes in Fig. 8b repeat roughly every three AOIs, which lines up with the slightly offset dots in Fig. 8a. The same spatial periodicity of approximately 3 lenslet sizes can be observed in Figure 1 for all statistical quantities.

## 3. AOI ERROR

In SHWFS dot patterns of the supersonic flow, the sharp gradients in density not only caused distorted dots, but also could push the dots to the edge of the AOIs, even crossing into the neighboring AOIs. So another source of error to consider is how close the dot is to the edge of the AOI. As more of the dot approaches the edge of the AOI, the centroid calculation underestimates the true centroid as the tails of the intensity distribution is no longer included in the calculations. For this study, we do not include pixelation effects and only consider the

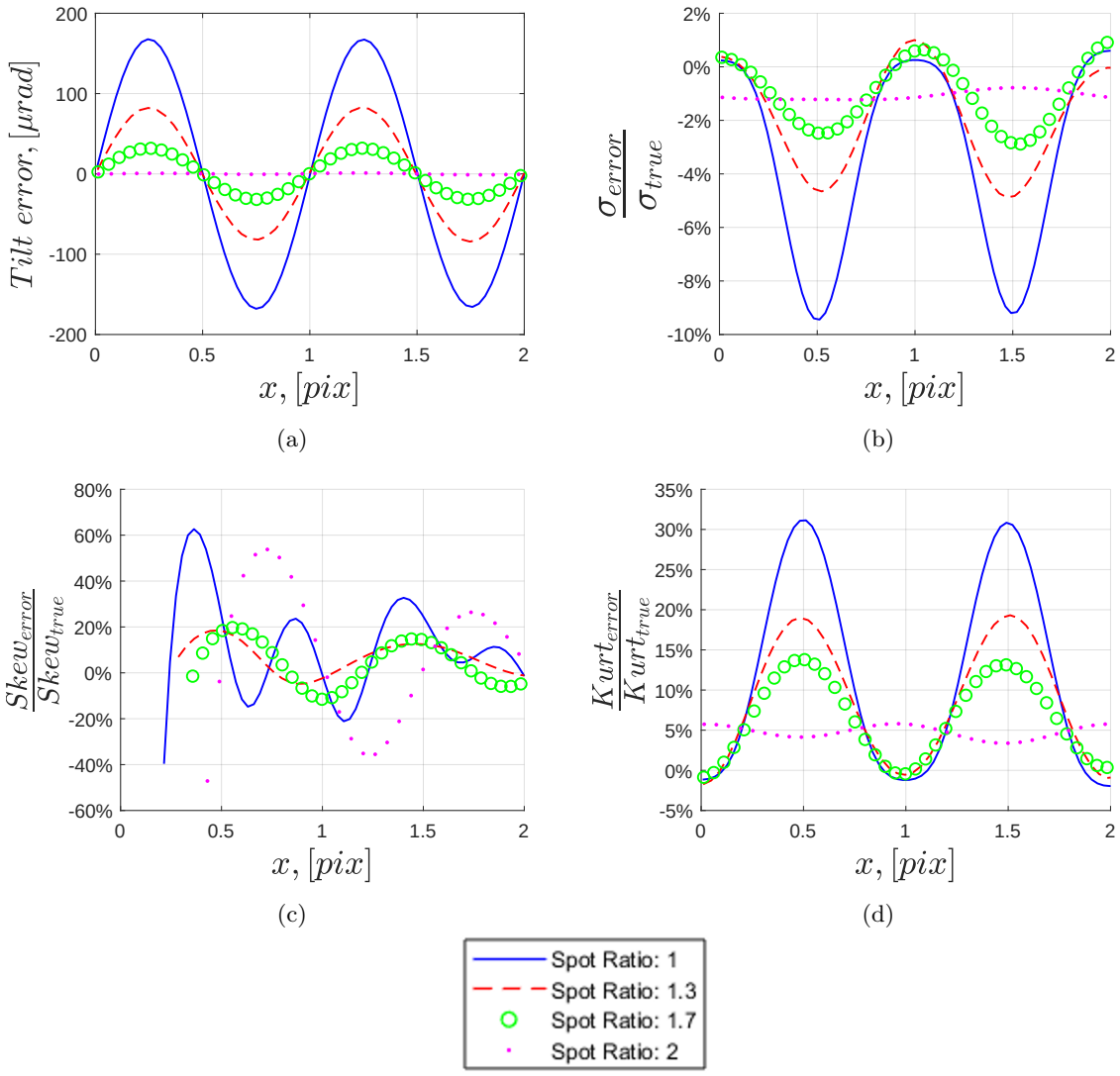



Figure 6: Plots shows the error of the (a) Centroid, and relative error of (b) $\sigma$, (c) $Skew$, and (d) $Kurt$ for when $\zeta_{pixel}$ =1, 1.3, 1.7, and 2.

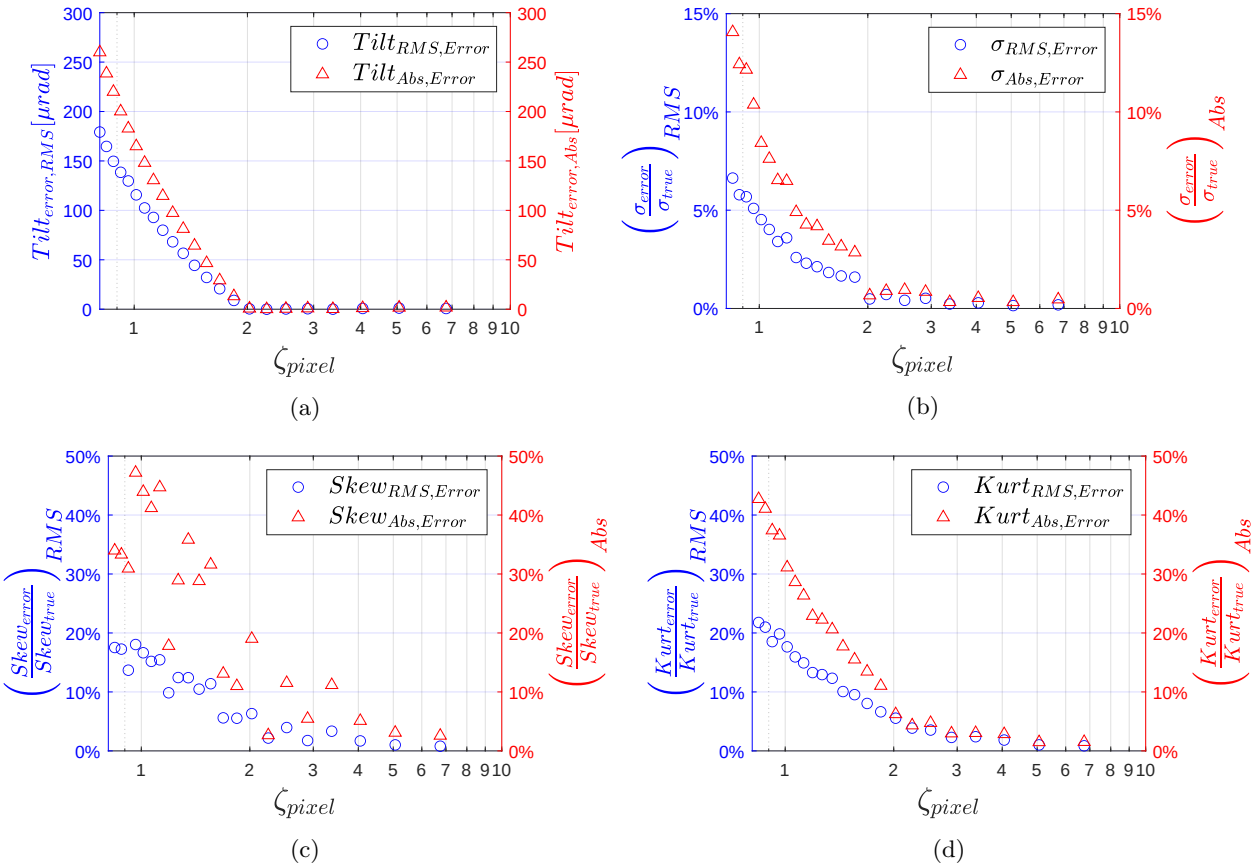
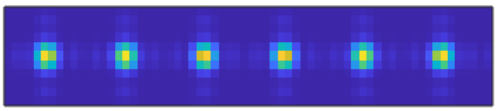
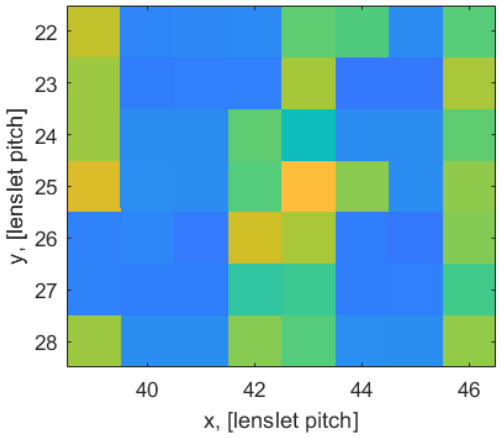



Figure 7: (a) The RMS tilt error and maximum tilt error both decrease towards $\zeta_{pixel} = 2$. (b) The RMS error and maximum error of $\sigma$. (c) The RMS error and maximum error of $Skew$. (d) The RMS error and maximum error of $Kurt$.



(a)




(b)

Figure 8: (a) Simulated dots showing how the slight mismatch between the lenslet array and the pixels in the camera creates a intensity distribution that is not completely centered within each AOI. (b) The $\sigma$ and $Kurt$ stripes that result from AOI-size to pixel-size mismatch. Each square represents an AOI.

position of the dot within the AOI. We introduce another parameter, $\zeta_{AOI}$, which describes the ratio between the size of the Dot peak and the size of the aperture, defined as

$$\zeta_{AOI} = \frac{L_{AOI}}{2W_x} \tag{9}$$

where $W_x$ the half-width of the dot and $L_{AOI}$ is the size of Area of Interest. Thus, at $\zeta_{AOI} = 1$, the size of the dot is the same as size of the AOI. In our experimental setup in Section 2.2, the SHWFS has a dot size of $2W_x = 135\mu m$ and a $L_{AOI} = 300\mu m$ giving a $\zeta_{AOI} = 2.2$. Fig. 9a the path of the calculated centroid for different $\zeta_{AOI}$ values compared to the true centroid (dashed black line). As the $\zeta_{AOI}$ increases, the path of the calculated centroid deviates less and less from the true centroid. The x-axis is the position of the calculated centroid, $\Delta x$, normalized by the half-width of the dot, $W_x$. It follows that a smaller dot (i.e. higher $\zeta_{AOI}$) allows more movement with less error within the AOI.

Nightingale et.al.[2] discusses gamma correction by raising the intensity distribution of the dot to a certain power. This increases the contrast between the center peak and the background noise. In this simulation, we squared and cubed the normalized intensity, given in Eq. 8, and calculated the centroid position. Fig. 9b and Fig. 9c show an improvement of the calculated centroid near the edge of the AOI. As a reminder to the reader, zero is the center of the AOI and $L_{AOI}$ is the size of the AOI as defined by the size of the lenslet, thus the edge of the AOI is half of $L_{AOI}$. $\Delta x$ is the distance moved from the center of the AOI.

Figures 10a, 10b, and 10c plot the same $\zeta_{AOI}$ but compares the relative error of squaring and cubing effect on the centroid for three different $\zeta_{AOI}$, where $\Delta x_{errror} = \Delta x_{calculated} - \Delta x_{true}$, $\Delta x_{calculated}$ is the calculated centroid for the averaged pixelated intensity and $\Delta x_{true}$ is the true deflection of the centroid of the dot from the center of the AOI. This shows that for a dot, without squaring the intensity, there is a significant error in the centroid calculation as the dot moves toward the edge. Our experimental system of $\zeta_{AOI} = 2.2$ is most closely represented by Fig. 10a. For the squared intensity, there is a significant increase in the error of the centroid at roughly 40% from the center of the AOI. Thus, the dynamic range of the dot is only 80% of the entire AOI before significant error begins to affect the calculated centroid.

Fig. 10d plots the maximum error for a regular, squared, and cubed intensity. Granted the maximum error always occurs at the edge of the AOI, the trend still shows the improvement from squaring the intensity. From these plots, cubing the intensity does not have a significant improvement of the error over squaring the intensity. Unless the dot is very close to the edge, the improvement is practically zero between squaring and cubing.

Thus there are two methods that help with reducing the error of dots near the edge of the AOI: (1) increasing the $\zeta_{AOI}$ ratio, (2) squaring or cubing the intensity distribution. The first method does allow for measurements of larger tilts, however, this is limited by the equipment as this ratio is a function of the size of the lenslets and wavelength of light used. This may not be feasible or expensive to change. Increasing the lenslet/AOI size will decrease the error but also reduces the spatial resolution of your wavefront measurements as now you are averaging the wavefront over a larger area. Thus the second method is much simpler and can be easily applied in post processing. Squaring and cubing the intensity distribution increases the contrast between the main dot and the smaller tails. This then improves the centroid calculations as the tails have less relative effect in calculating the centroid. However, past squaring the intensity does not seem to decrease the error in any significant capacity.

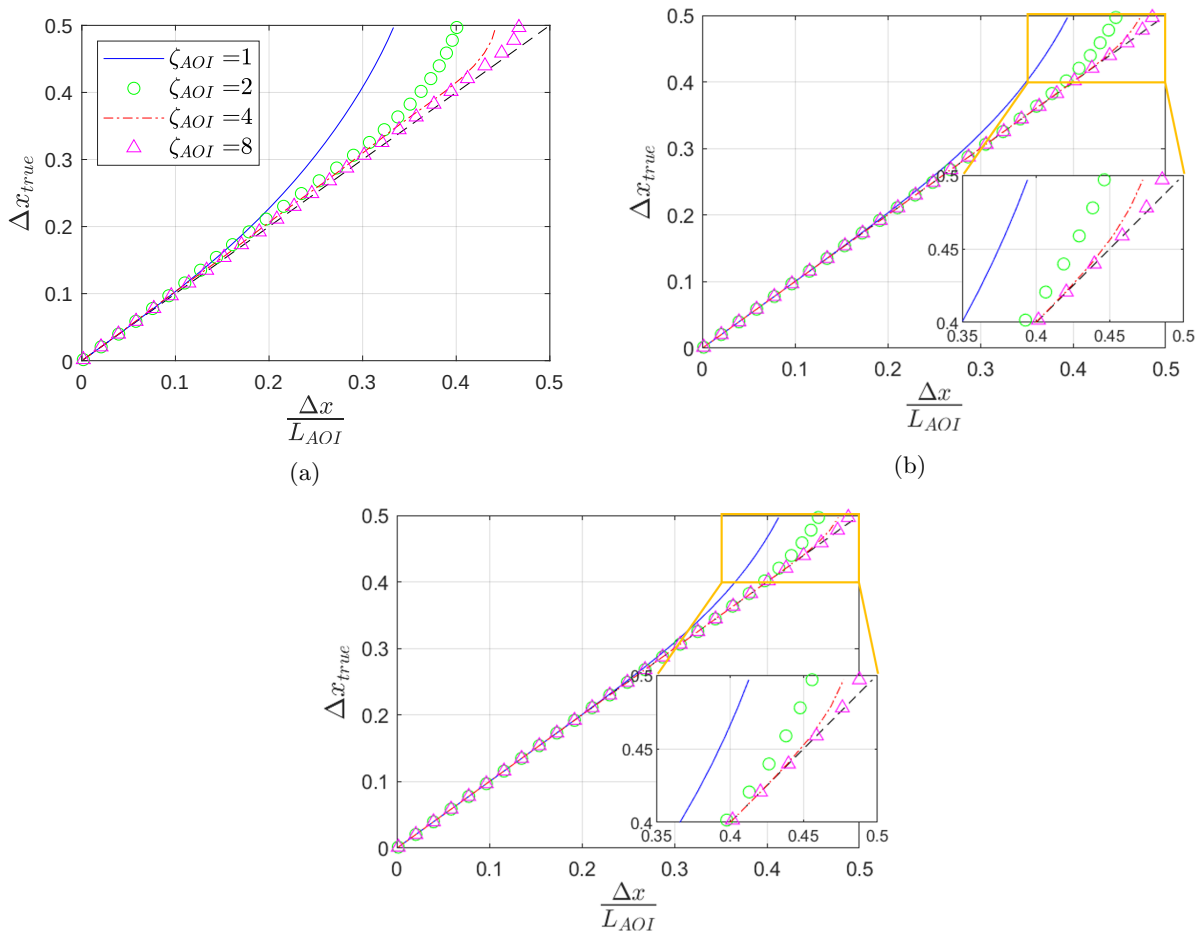



Figure 9: AOI error as a function of $\zeta_{AOI}$. (a) The calculated centroid is plotted against the true centroid position the normalized intensity. The normalized intensity is (b) squared and (c) cubed, which shows the calculated centroid to be closer to the true centroid near the edge of the AOI

.

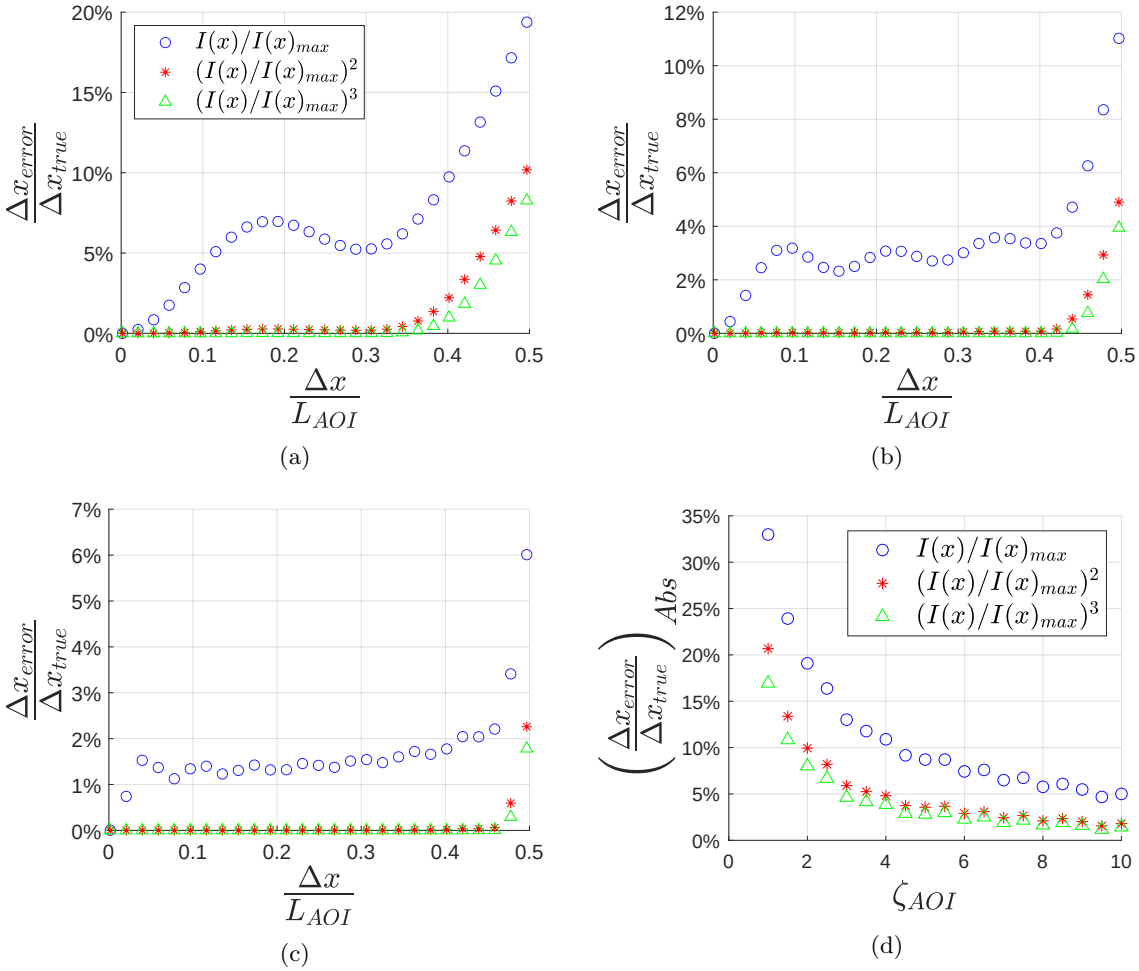



Figure 10: Relative AOI error as a function of squaring and cubing the normalized intensity distribution for (a) $\zeta_{AOI} = 2$, (b) $\zeta_{AOI} = 4$, (c) $\zeta_{AOI} = 8$. (d) Maximum relative error comparing the regular, squared, and cubed intensity distributions

.

## 4. CONCLUSION AND DISCUSSION

In previous work, we used a Shack-Hartmann Wavefront sensor (SHWFS) to capture a shock in supersonic flow. The shock is a sudden change in density in the air which distorted the dots in the SHWFS which then causes inaccurate centroid calculations. By using standard deviation and kurtosis statistics of the individual dot intensity pattern, we can identify and remove distorted dots affected by supersonic shocks. However, on these statistic maps, stripes were observed that were not related to the flow. We suspected that this was due to the nature of the finite pixels of the digital camera. In the first part of this study, we explored how the pixelation of a diffraction limited dot would affect the centroid, standard deviation ($\sigma$), skewness ($Skew$), and kurtotsis ($Kurt$). We performed a simulation of a ideal double sinc dot intensity, averaged the intensity across different pixel sizes and calculated the centroid, $\sigma$, $Skew$ and $Kurt$ values. Taking the difference between the pixelated distribution and the true values, we observed an oscillating error which converges to zero as the pixel size decreases. To describe the relationship between a diffraction limited dot and the pixel width, we introduce $\zeta_{pixel}$ which describes the ratio between the width of the center dot peak and the camera pixel. This describes how many pixels are needed to fully capture the center peak of a diffraction limited dot. We found that at $\zeta_{pixel} = 2$ reduces the centroid error to near zero and also greatly reduces the relative error of $\sigma$ and $Kurt$ of a pixel averaged dot. The stripes that were observed on the statistics maps were determined to be caused by the mismatch of the size of the Area of Interest (AOI) and the size of the pixel used by the camera. This results in the pixels to slightly skew the intensity distribution every 3 AOIs which in turn caused the $\sigma$ and $Kurt$ values to be higher in those AOIs.

In the second part of this study, we looked at the centroid error of a dot that approaches the edge of the AOI. While capturing the supersonic flow, the sharp density gradients can also push the dots to the edge of the AOI, even crossing over to the neighboring AOIs. We introduced another parameter, $\zeta_{AOI}$ which is the ratio of the AOI size and the dot size. Ideally, a large $\zeta_{AOI}$ ratio is desired as that allows for the most tilt and movement within the AOI. However, this is not always possible due to equipment limitations. Thus another method of increasing the range of tilt is by squaring or cubing the intensity distribution. This increases the contrast between the center dot peak and the tails of the intensity. As such, the tails have less impact on the centroid calculations even if they move past the AOI. In future work, we seek to optimize the Dot-size/pixel-size ratio and the AOI-size/dot-size to achieve the least error for our given system.

## 5. ACKNOWLEDGEMENTS

The authors would like to thank Tim Bukowski for discussions and work in simulations which has been extremely helpful in this study.

This work was partially funded by the Aerospace and Mechanical Engineering Department at the University of Notre Dame.

## REFERENCES


[1] Chu, E. D., Bukowski, T. J., and Gordeyev, S., "Studies of local shock effects on Shack-Hartmann and digital holography wavefront sensors," in [*Unconventional Imaging, Sensing, and Adaptive Optics 2023*], Dolne, J. J., Spencer, M. F., and Bose-Pillai, S. R., eds., **12693**, 1269317, International Society for Optics and Photonics, SPIE (2023).

[2] Nightengale, A. M. and Gordeyev, S., "Shack-hartmann wavefront sensor image analysis: a comparison of centroiding methods and image-processing," *Optical Engineering* **52(7)**, 071413 (2013).

[3] Merritt, P. and Spencer, M., [*Beam Control for Laser Systems*], The Directed Energy Professional Society, Wiley (2018).

[4] Feng, F., Liang, C., Chen, D., Du, K., Yang, R., Lu, C., Chen, S., He, W., Xu, P., Chen, L., Tao, L., and Mao, H., "Moment-based space-variant shack–hartmann wavefront reconstruction," *Optics Communications* **540**, 129515 (2023).

[5] Gordeyev, S., Burns, R., Jumper, E., Gogineni, S., Paul, M., and Wittich, D., "Aero-optical mitigation of shocks around turrets at transonic speeds using passive flow control," in [*51st AIAA Aerospace Sciences Meeting including the New Horizons Forum and Aerospace Exposition*], Grapevine, TX, AIAA Paper 2013-0717 (June 2013).

[6] Panda, J. and Adamovsky, G., "Laser light scattering by shock waves," *Physics of Fluids* **7**, 2271–2279 (09 1995).

[7] Kemnetz, M., Kalensky, M., Roeder, A., and Noel, Z., "Effects of shock-related discontinuities on SHWFS measurements: experimental results (Conference Presentation)," in [*Unconventional Imaging and Adaptive Optics 2022*], Dolne, J. J. and Spencer, M. F., eds., **12239**, 122390I, International Society for Optics and Photonics, SPIE (2022).

[8] Kemnetz, M. R., Kalensky, M., DeFoor, T. E., and Spencer, M. F., "Experimental investigation into the effects of shock waves on Shack-Hartmann wavefront sensor measurements," in [*Unconventional Imaging, Sensing, and Adaptive Optics 2023*], Dolne, J. J., Spencer, M. F., and Bose-Pillai, S. R., eds., **12693**, 1269314, International Society for Optics and Photonics, SPIE (2023).

[9] Kalensky, M., Kemnetz, M. R., and Spencer, M. F., "Effects of shock waves on shack–hartmann wavefront sensor data," *AIAA Journal* **61**, 2356–2368 (May 2023).